

# DivCon-NeRF: Generating Augmented Rays with Diversity and Consistency for Few-shot View Synthesis

Ingyun Lee

Jae Won Jang

Seunghyeon Seo

Nojun Kwak

Seoul National University

{ig.lee, pert0407, zzzlssh, nojunk}@snu.ac.kr

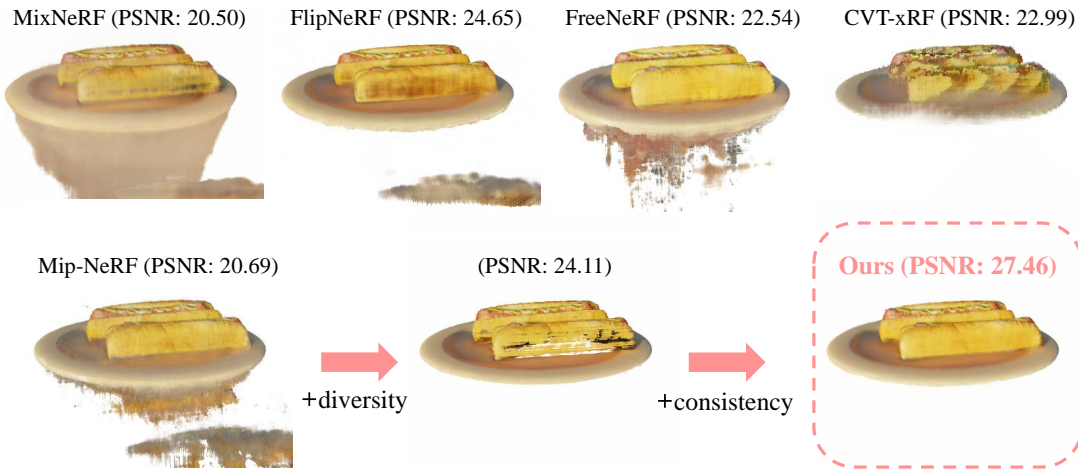


Figure 1. **Rendering results of recent methods in the hotdog scene of the Blender dataset with 4 views.** Notable floaters and appearance distortions are visible in the results of other state-of-the-art approaches. Our method effectively addresses these issues by simultaneously considering diversity and consistency.

## Abstract

Neural Radiance Field (NeRF) has shown remarkable performance in novel view synthesis but requires many multi-view images, making it impractical for few-shot scenarios. Ray augmentation was proposed to prevent overfitting for sparse training data by generating additional rays. However, existing methods, which generate augmented rays only near the original rays, produce severe floaters and appearance distortion due to limited viewpoints and inconsistent rays obstructed by nearby obstacles and complex surfaces. To address these problems, we propose DivCon-NeRF, which significantly enhances both diversity and consistency. It employs surface-sphere augmentation, which preserves the distance between the original camera and the predicted surface point. This allows the model to compare the order of high-probability surface points and filter out inconsistent rays easily without requiring the exact depth. By introducing inner-sphere augmentation, DivCon-NeRF randomizes angles and distances for diverse viewpoints, further increasing diversity. Consequently, our method significantly reduces floaters and visual distortions, achiev-

ing state-of-the-art performance on the Blender, LLFF, and DTU datasets. Our code will be publicly available.

## 1. Introduction

Deep learning has been actively explored for various 3D computer vision applications. Among them, novel view synthesis, which generates new views of a scene from input images, has seen substantial advancements. In particular, Neural Radiance Field (NeRF) [27], a neural network-based approach, has significantly improved performance in this area. However, NeRF-based models suffer from the typical deep learning challenge of performance degradation in few-shot scenarios. A limited number of training rays with sparse viewpoints causes overfitting. Therefore, the need for numerous images from different angles presents a substantial challenge in the practical applications of NeRF-based models. To address the few-shot view synthesis problem, three main approaches are being actively researched: prior-based, framework-based, and regularization-based methods, respectively. Each approach

takes different directions and is relatively orthogonal. Prior-based methods [4, 41, 48] rely on pre-training large-scale datasets to leverage 3D knowledge, but these methods result in high computational costs. On the other hand, framework-based methods [52, 53] modify or extend model architectures, which can increase model complexity.

Our method can be categorized as a regularization-based method, which optimizes each scene individually utilizing regularization terms [13, 47] or additional training sources [10]. Ray augmentation, one of the regularization-based methods, generates augmented rays from a small set of training rays, allowing the model to train on both original and augmented rays to mitigate overfitting. Ray augmentation directly addresses the issue of insufficient training rays by increasing their number, providing an effective solution. Existing ray augmentation methods [34, 35] generate augmented rays only near the original rays to reduce the likelihood of being occluded by obstacles. However, as shown in Fig. 1, these approaches suffer from severe floaters due to limited viewpoint variation and training on inconsistent rays obstructed by nearby obstacles and complex surfaces. They also introduce geometric and color distortions.

To address the limitations of existing methods, we propose DivCon-NeRF, which enhances diversity while preserving consistency. In general data augmentation, many studies [8, 9, 12, 21, 45] focus on diversifying data while maintaining consistency. Based on this observation, we hypothesize that increasing diversity and maintaining ray consistency are crucial for performance in few-shot view synthesis. To achieve this, DivCon-NeRF consists of surface-sphere augmentation and inner-sphere augmentation. As shown in Fig. 1, our method effectively reduces floaters and appearance distortions.

To achieve higher-quality few-shot synthesis, we define a 3D sphere centered at the object’s inferred surface point with a radius equal to the distance between the camera and the inferred surface point. We cast augmented rays from the sphere’s surface and within the sphere, both directed toward the inferred surface point. To be consistent with the original ray, the model should predict the same surface point for augmented rays reaching the same location. In surface-sphere augmentation, we create a consistency mask by comparing the order of high-probability surface points between the original and augmented rays, allowing the model to filter out inconsistent rays easily without requiring precise rendered depth. We propose a ray consistency loss that aligns surface points by comparing the similarity of blending weight distributions, where a temperature factor is applied to give more weight to regions with higher surface probabilities. Additionally, we introduce a positional constraint to the bottleneck feature loss that accounts for the relative positional relationships of points. For greater diversity, inner-sphere augmentation utilizes both randomized angles and

distances, providing a broader range of viewpoints.

Our DivCon-NeRF effectively increases diversity while maintaining consistency, resulting in improved rendering quality compared with other state-of-the-art (SOTA) methods. These results support our hypothesis that both diversity and consistency are crucial for enhancing rendering performance. Our main contributions are as follows:

- We experimentally demonstrate the importance of diversity and consistency in ray augmentation, analyzing their effects across object-centric scenes and scenes with diverse depth ranges.
- We propose DivCon-NeRF, a novel ray augmentation method that simultaneously enhances diversity and preserves consistency.
- Our DivCon-NeRF significantly reduces floaters and appearance distortions, achieving SOTA performance on the Blender, LLFF, and DTU datasets.
- Our method can be combined with other regularization- and framework-based methods, demonstrating its generalizability.

## 2. Related work

### 2.1. Neural scene representations

Neural scene representations have become a prominent method for encoding 3D scenes, showing impressive results in tasks like novel view synthesis [3, 27–29] and 3D scene generation [14, 24, 33]. These methods typically leverage neural networks to model scene properties continuously rather than relying on traditional discretized representations, such as meshes [17, 23, 31], voxels [11, 43, 44, 49], or point clouds [1, 37]. Neural scene representations enable highly detailed and photorealistic reconstructions of scenes [25, 32]. Among the various approaches, NeRF [27] has gained attention for its ability to synthesize novel views. However, NeRF-based models suffer from a significant drop in performance with sparse training images [36, 48].

### 2.2. Few-shot view synthesis

Various approaches have been researched to address few-shot view synthesis in NeRF-based models. Prior-based methods [4, 16, 48] pre-train models on large-scale datasets to provide prior knowledge of 3D scenes. However, these methods incur substantial costs due to large-scale datasets and pre-training, and performance can degrade significantly when the distribution of the pre-training dataset differs from that of the training dataset [34].

Framework-based methods modify network structures with models such as Transformers [39] and CNNs [19], and use these modified models during rendering. mi-MLP [53] incorporates input embeddings into each MLP layer for flexible learning, while CVT-xRF [52] employs an in-voxel Transformer to refine radiance properties within voxels.

However, these methods increase model complexity and hinder integration with other framework-based methods. Additionally, appearance distortions persist due to sparse viewpoint, as shown in Fig. 1.

Regularization-based methods optimize each scene using regularization terms [13] or additional training sources [10]. SparseNeRF [40] introduces a local depth ranking regularization to enhance depth consistency. FreeNeRF [47] implements a frequency domain to mitigate artifacts. However, data scarcity remains unresolved, as these methods do not directly increase the number of training images, leading to several floaters, as shown in Fig. 1.

Additionally, separate from NeRF, recent few-shot 3D Gaussian Splatting (3DGS) methods [22, 50, 54] have demonstrated strong performance in general cases. However, they struggle significantly in background-free scenes crucial for practical applications such as advertising. In contrast, we show how our method excels in these scenarios.

### 2.3. Ray augmentation for sparse images

Ray augmentation is a regularization-based approach that generates augmented rays from the original ones. This approach [6, 35, 38] effectively addresses the shortage of training rays by directly increasing their quantity. InfoNeRF [18] reduces ray entropy, aiding in consistency across close views, while RegNeRF [30] simulates unobserved viewpoints to refine the geometry and appearance. FlipNeRF [34] employs flipped reflection rays to improve 3D geometry estimation. However, these methods, which augment rays only around the original ones, struggle with complex surfaces and nearby obstacles, causing inconsistencies. Furthermore, these methods utilize augmented rays from limited viewpoints. GeCoNeRF [20] applies a depth mask to every pixel of a warped patch rather than directly to a ray. This mask assumes the use of image warping, which causes interpolation issues and fails to maintain equal distances from surface points to both the original and pseudo cameras for each pixel, resulting in coarse filtering. Therefore, GeCoNeRF [20] still relies on pseudo-views close to the training views. Consequently, these limitations of existing methods lead to severe floaters and appearance distortions due to low diversity and inadequate consistency. In contrast, our method enhances both diversity and consistency, effectively addressing these limitations.

### 3. Preliminaries: NeRF

NeRF [27] utilizes MLPs to synthesize novel views of a scene from dense images. The input of NeRF network  $F$  includes the 3D coordinates  $\mathbf{X} = (x, y, z)$  of points located along a camera ray and the viewing direction  $\mathbf{d}$ . The output is the emitted color  $\mathbf{c}$  and the volume density  $\sigma$  at each point:

$$F : (\mathbf{x}, \mathbf{d}) \rightarrow (\mathbf{c}, \sigma). \quad (1)$$

Conceptually, NeRF casts a single ray into 3D space for each pixel in the image. Since the ray is continuous, points along the ray are sampled. The results from these points are accumulated to determine the final color  $C$  of the pixel. The ray can be expressed as  $\mathbf{r}(t) = \mathbf{O} + t\mathbf{d}$ , where  $\mathbf{O}$  represents the camera coordinates. The predicted pixel color  $C(\mathbf{r})$  is calculated as follows:

$$C(\mathbf{r}) = \sum_{i=1}^N T_i (1 - \exp(-\sigma_i \delta_i)) \mathbf{c}_i = \sum_{i=1}^N w_i \mathbf{c}_i, \quad (2)$$

where  $T_i = \exp\left(-\sum_{j=1}^{i-1} \sigma_j \delta_j\right)$ , and  $\delta_i = t_{i+1} - t_i$ . Blending weight  $w_i = T_i (1 - \exp(-\sigma_i \delta_i))$  represents the contribution of the color at the  $i$ -th point to the blended color  $C(\mathbf{r})$ . The NeRF network  $F$  is optimized using a mean square error (MSE) loss to ensure that the predicted pixel colors match the ground truth colors of the training rays:

$$\mathcal{L}_{\text{MSE}} = \sum \|C_{\text{gt}}(\mathbf{r}) - C(\mathbf{r})\|^2, \quad (3)$$

where  $C_{\text{gt}}(\mathbf{r})$  denotes the ground truth color of the training ray. NeRF performs exceptionally well when sufficient training data is available, but as with most deep learning models, its performance significantly degrades when the training data is limited.

## 4. Method

We propose DivCon-NeRF, a ray augmentation method that focuses both on enhancing ray diversity and preserving ray consistency. Unlike depth-based image warping methods [5, 20], DivCon-NeRF augments rays directly in 3D space. The method includes surface-sphere augmentation (Sec. 4.1), which generates new rays on a sphere, and inner-sphere augmentation (Sec. 4.2), which introduces random variations in distance within the sphere, both directed toward the inferred surface point of the original ray. In surface-sphere augmentation, a progressive consistency mask filters out inconsistent rays, and two losses refine the alignment between the augmented and original rays. In inner-sphere augmentation, rays from various viewpoints are generated and utilized for robust training. The overall scheme of our DivCon-NeRF is depicted in Fig. 2.

### 4.1. Surface-sphere augmentation

Unlike the typical approach [27], where the center of a virtual sphere is positioned at the center of the object or 3D scene to determine camera positions, we use a virtual sphere centered on the predicted surface point  $\mathbf{P}_s$  where the original ray hits. When the original and augmented rays cast from the sphere intersect at the same surface point, this condition indicates that the augmented ray is unobstructed. We verify the consistency of the augmented rays by comparing the surface points hit by both rays.

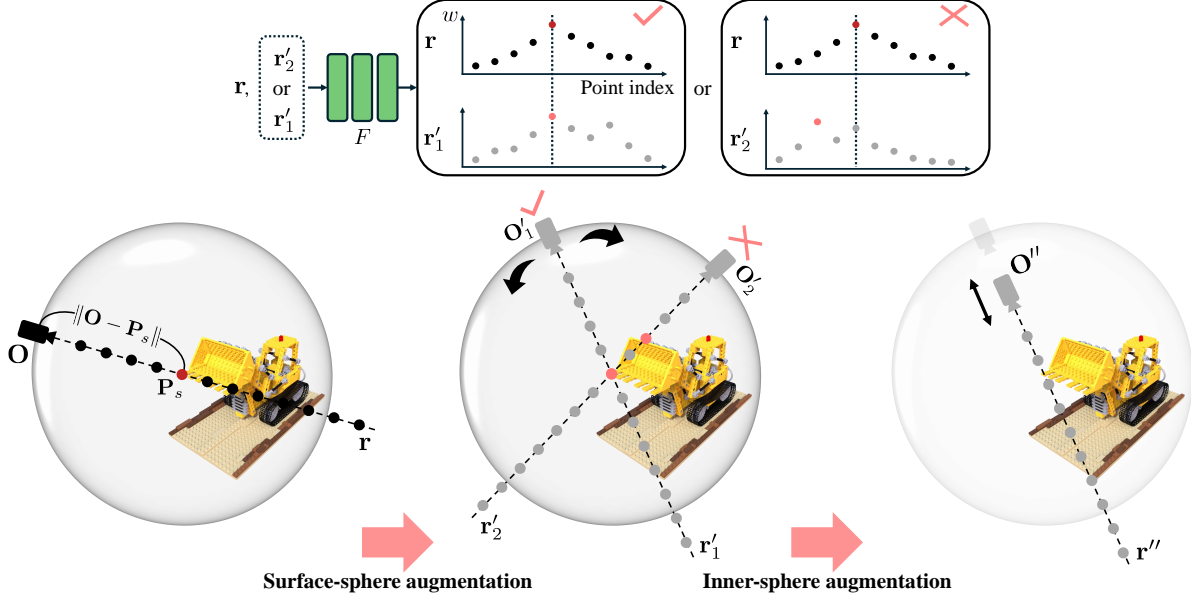


Figure 2. **Overall structure of DivCon-NeRF.** (Left) First, the virtual sphere is defined, centered at the predicted surface point  $\mathbf{P}_s$ . (Center) A surface-sphere augmented ray  $\mathbf{r}'$  is then cast from a randomly selected position on the sphere’s surface. (Right) To further enhance diversity, an inner-sphere augmented ray  $\mathbf{r}''$  is generated with a randomly selected radius within the sphere and the same random angle as the surface-sphere augmented ray. (Top) To maintain consistency, the consistency mask filters out inconsistent rays (e.g.  $\mathbf{r}'_2$ ) if the sampled point with the highest blending weight does not have the same index as the original.

For surface-sphere augmentation, the sphere’s center and radius must be determined. The center is located at  $\mathbf{P}_s$ , the most likely surface point predicted by the model:  $\mathbf{P}_s = \mathbf{O} + t_s \mathbf{d}$ , where  $s = \operatorname{argmax}_i (w_i)$ . The radius is calculated as  $\|\mathbf{O} - \mathbf{P}_s\|$ . Consequently, the augmented ray’s camera coordinates  $\mathbf{O}'$  are given by:

$$\begin{aligned} x_{o'} &= \|\mathbf{O} - \mathbf{P}_s\| \sin(\theta) \cos(\phi), \\ y_{o'} &= \|\mathbf{O} - \mathbf{P}_s\| \sin(\theta) \sin(\phi), \\ z_{o'} &= \|\mathbf{O} - \mathbf{P}_s\| \cos(\theta), \end{aligned} \quad (4)$$

where  $(\theta, \phi)$  are spherical coordinates, with  $\theta \sim U[0, \pi]$  and  $\phi \sim U[0, 2\pi)$ .

During training, the model progressively improves its prediction of  $\mathbf{P}_s$ , refining the accuracy of the virtual sphere. Importantly, no matter which point on the sphere an augmented ray is cast from, all rays have the same distance  $R$  ( $= t_s \|\mathbf{d}\|$ ) and will converge toward  $\mathbf{P}_s$ . With this characteristic of surface-sphere augmentation, a consistency mask can be obtained by simply estimating the order of the blending weights  $w_i$ ’s along the ray rather than precisely predicting the depth.

#### 4.1.1. Consistency mask

To generate the consistency mask for augmented rays without restricting angle and distance, we consider all points on the virtual sphere as potential positions for  $\mathbf{O}'$ . In each iteration, we randomly select a point on the sphere as  $\mathbf{O}'$  for

each original ray. The coordinates of the sampled points along the surface-sphere augmented ray are computed as  $\mathbf{r}'(t) = \mathbf{O}' + t \mathbf{d}'$ , where  $\mathbf{d}'$  denotes the augmented ray’s camera viewing direction, which is calculated as follows:

$$\mathbf{d}' = \frac{\|\mathbf{d}\| (\mathbf{P}_s - \mathbf{O}')}{\|\mathbf{P}_s - \mathbf{O}'\|} \quad (5)$$

The magnitude of  $\mathbf{d}'$  is set to be equal to  $\mathbf{d}$  to match the distribution of the original training data. The sampled points along the augmented ray are fed into the model  $F$ . The point with the highest blending weight is identified as the most likely surface point along the augmented ray:  $\mathbf{P}_{s'} = \mathbf{O}' + t_{s'} \mathbf{d}'$ , where  $s' = \operatorname{argmax}_i (w'_i)$ , with the blending weight  $w'_i$  derived from the augmented ray. Note that this process occurs during coarse sampling, where points are sampled at equal intervals. Because  $\|\mathbf{P}_s - \mathbf{O}\| = \|\mathbf{P}_s - \mathbf{O}'\|$  and  $\delta = \delta'$ , where  $\delta$  and  $\delta'$  represent the distances between adjacent samples on the original and augmented rays, respectively,  $\mathbf{P}_{s'}$  of the consistent ray should be identical to  $\mathbf{P}_s$ . To exclude occluded rays from training, we define the following consistency mask:

$$M(\mathbf{r}, \mathbf{r}') = \begin{cases} 1 & \text{if } |s - s'| \leq \epsilon \\ 0 & \text{otherwise,} \end{cases} \quad (6)$$

where  $\mathbf{r}'$  refers to the surface-sphere augmented ray derived from the original ray  $\mathbf{r}$  and  $s/s'$  is the point index at

which the blending weight is the highest along the ray  $\mathbf{r}/\mathbf{r}'$ , *i.e.*,  $s/s' = \operatorname{argmax}_i (w_i/w'_i)$ . We introduce the parameter  $\epsilon$  as an error tolerance, given that this process occurs during coarse sampling. If the difference between the indices exceeds  $\epsilon$ , the augmented ray is filtered out, indicating that the ray reaches a different surface point.

Accurately estimating  $w_i$  and  $w'_i$  at every point is challenging for a model without pre-training. For example, GeCoNeRF [20], which uses depth for masking warped patches, employs an additional depth smoothness loss to obtain more accurate rendered depth. However, determining the point with the highest blending weight via the  $\operatorname{argmax}$  function is relatively easier, even for a model in training.

#### 4.1.2. Ray consistency loss

Besides the consistency mask, we propose a ray consistency loss to further align the surface points of  $\mathbf{r}$  and  $\mathbf{r}'$ , thereby improving overall consistency. To reinforce this alignment, we increase the similarity between the blending weight distribution  $w$  of the original ray and  $w'$  of the augmented ray. Our goal is not merely to match the similarity of these distributions but also to ensure their blending weights peak at the same surface point. Augmented rays far from the original rays should not exhibit high similarity of overall distribution but should show greater similarity near the surface.

We reduce the weights of points where  $w_i$  and  $w'_i$  are smaller while increasing the weights where these values are larger. To sharpen the distributions, we apply a temperature  $T$ . The similarity of the sharpened distributions is measured using KL divergence. The ray consistency loss for each ray is defined as:

$$l_{RC}(\mathbf{r}, \mathbf{r}') = KL(P_T \| Q_T), \quad (7)$$

where

$$P_T(i) = \frac{\exp(w_i/T)}{\sum_j \exp(w_j/T)} \text{ and } Q_T(i) = \frac{\exp(w'_i/T)}{\sum_j \exp(w'_j/T)}.$$

For the LLFF [26] dataset, which contains many objects within a scene, augmented rays farther from the original rays tend to have more dissimilar overall distributions. For these augmented rays located beyond a certain range, we apply clipping to  $w_i$  and  $w'_i$  by setting them to 0 when  $i > s$  and then obtain  $P_T(i)$  and  $Q_T(i)$ . Finally, the overall ray consistency loss  $\mathcal{L}_{RC}$  for the entire set of rays  $\mathcal{R}$  is defined as:

$$\mathcal{L}_{RC} = \sum_{\mathbf{r} \in \mathcal{R}} M(\mathbf{r}, \mathbf{r}') \cdot l_{RC}(\mathbf{r}, \mathbf{r}'). \quad (8)$$

Unlike InfoNeRF [18], which only applies information regularization to augmented rays with minimal viewpoint variations, our approach leverages temperature and clipping to enforce a strong consistency constraint near the surface, utilizing augmented rays across all ranges for  $\mathcal{L}_{RC}$ . Further comparison experiments are detailed in the supplementary material.

#### 4.1.3. Positional bottleneck feature loss

We introduce a positional constraint to the bottleneck feature loss proposed in FlipNeRF [34]. Unlike FlipNeRF, which does not maintain a consistent positional relationship among sampled points due to the varying magnitudes of normal vectors, we utilize sampled points from the original and augmented rays that are equidistant from the predicted surface point. Positional bottleneck feature loss is calculated by Jensen-Shannon divergence, as shown below:

$$l_{PBF}(\mathbf{r}, \mathbf{r}') = \sum_{i=1}^N \frac{1}{N} JSD(\psi(h(\mathbf{X}_i)), \psi(h(\mathbf{X}'_i))), \quad (9)$$

where  $\|\mathbf{P}_s - \mathbf{X}_i\| = \|\mathbf{P}_s - \mathbf{X}'_i\|$ ,  $\psi$  denotes the softmax function, and  $h(\cdot)$  maps input to the last layer’s feature space. This constraint reduces geometric differences between  $\mathbf{X}_i$  and  $\mathbf{X}'_i$  for reliable feature matching, as demonstrated in Sec. 5.3. Therefore, we obtain  $l_{PBF}$  through the coarse sampling of surface-sphere augmentation, not the inner-sphere augmentation. The overall positional bottleneck feature loss  $\mathcal{L}_{PBF}$  across the entire set of rays  $\mathcal{R}$  is defined as:

$$\mathcal{L}_{PBF} = \sum_{\mathbf{r} \in \mathcal{R}} M(\mathbf{r}, \mathbf{r}') \cdot l_{PBF}(\mathbf{r}, \mathbf{r}'). \quad (10)$$

## 4.2. Inner-sphere augmentation

In addition to surface-sphere augmentation, we also randomly select the distance  $R$  within the sphere in each iteration for inner-sphere augmentation, further enhancing diversity and making the model robust to variations in the camera’s distance from the surface. When a pseudo camera position is farther from the surface point than the original camera, a single pixel must represent a larger area, covering both the ground truth and its neighboring pixels, which makes maintaining color consistency more challenging. Therefore, the inner-sphere augmented ray’s camera coordinates  $\mathbf{O}''$  are given by:

$$\begin{aligned} x_{o''} &= r \|\mathbf{O} - \mathbf{P}_s\| \sin(\theta) \cos(\phi) \\ y_{o''} &= r \|\mathbf{O} - \mathbf{P}_s\| \sin(\theta) \sin(\phi) \\ z_{o''} &= r \|\mathbf{O} - \mathbf{P}_s\| \cos(\theta), \end{aligned} \quad (11)$$

where  $r \sim U(0, 1]$ , and  $\theta$  and  $\phi$  are common random variables shared with surface-sphere augmentation, resulting in the same viewing direction as  $\mathbf{d}'$ . Therefore, we can apply the same consistency mask, as it detects the presence of obstacles within the sphere along the line containing both augmented rays. This approach may filter out a few consistent rays but significantly reduces the likelihood of training on inconsistent rays.

The predicted color from the inner-sphere augmented ray is used to maintain color consistency by employing the neg-

ative log-likelihood (NLL) loss from MixNeRF [35]:

$$\mathcal{L}_{\text{MNLL}} = - \sum_{\mathbf{r} \in \mathcal{R}} M(\mathbf{r}, \mathbf{r}') \cdot \log p(C_{\text{gt}} | \mathbf{r}''), \quad (12)$$

where  $C_{\text{gt}}$  is the ground truth color of the original ray,  $\mathbf{r}''$  is the inner-sphere augmented ray derived from  $\mathbf{r}$ , and  $p(C | \mathbf{r}) = \sum_{i=1}^N \pi_i \mathcal{F}(C | \mathbf{r})$ . Here,  $\pi_i = \frac{w_i}{\sum_{m=1}^N w_m}$  and  $\mathcal{F}$  denotes a Laplacian distribution. Even though the rays converge at the same surface point, the consistent augmented ray does not necessarily have the same ground truth color as the original ray due to view-dependent effects. Therefore, we model the augmented ray to maintain a visually consistent color that adapts naturally across views, preserving a coherent and stable appearance. By utilizing a probability-based NLL loss and applying this augmentation during coarse sampling, the model is encouraged to predict consistent colors with  $C_{\text{gt}}$  from different viewpoints, resulting in smoother renderings.

### 4.3. DivCon-NeRF

DivCon-NeRF combines surface-sphere augmentation and inner-sphere augmentation, which work together to maintain consistency and enhance diversity for robust training. The overall training loss is defined as follows, with  $\lambda$  terms representing balancing weights for the respective losses:

$$\begin{aligned} \mathcal{L} = & \mathcal{L}_{\text{MSE}} + \lambda_1 \mathcal{L}_{\text{RC}} + \lambda_2 \mathcal{L}_{\text{PBF}} \\ & + \lambda_3 \mathcal{L}_{\text{MNLL}} + \lambda_4 \mathcal{L}_{\text{NLL}} + \lambda_5 \mathcal{L}_{\text{UE}}. \end{aligned} \quad (13)$$

Here,  $\mathcal{L}_{\text{MSE}}$  is calculated using the original ray.  $\mathcal{L}_{\text{NLL}}$  is the NLL loss of the original ray, introduced in MixNeRF [35], and  $\mathcal{L}_{\text{UE}}$  refers to the uncertainty-aware emptiness loss introduced in FlipNeRF [34], stabilizing the blending weights to prevent fluctuations. The supplementary material provides more details of both losses.

## 5. Experiments

### 5.1. Datasets and metrics

We compare our method with various SOTA approaches across the Blender [27], LLFF [26], and DTU [15] datasets. Blender includes 8 synthetic object-centric scenes without background. LLFF consists of 8 real-world scenes that face forward. We use 15 scenes among the 124 scenes in the DTU dataset, following RegNeRF’s [30] protocol.

We report PSNR, SSIM [42], LPIPS [51], and the average error (AVGE) calculated as the geometric mean of  $\text{MSE} = 10^{-\text{PSNR}/10}$ ,  $\sqrt{1 - \text{SSIM}}$ , and LPIPS, following [30]. LPIPS is measured using AlexNet [19], following [34, 35, 52]. More details of the experimental setup and implementation can be found in the supplementary material.

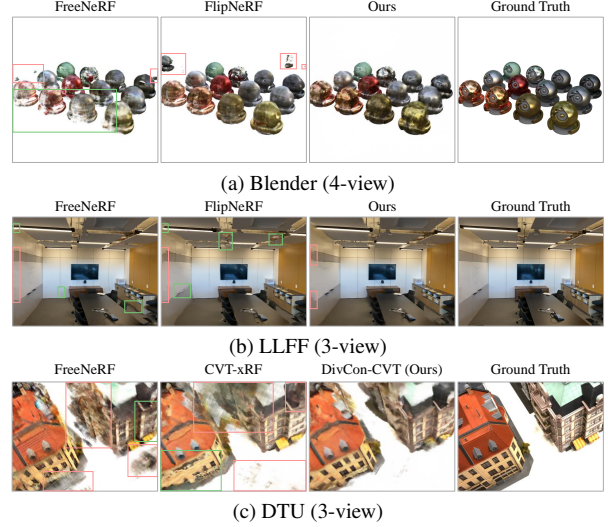


Figure 3. **Qualitative comparisons on Blender, LLFF, and DTU.** Red boxes indicate severe floaters and green boxes indicate significant visual distortions. Our method exhibits fewer floaters and visual distortions than other SOTA methods across all three datasets.

### 5.2. Comparison with state-of-the-art methods

**Blender.** Our method significantly outperforms all other SOTA approaches on the Blender dataset, as shown in Tab. 1. For a fair comparison, we follow the experimental settings of MixNeRF [35] (no mark) and DietNeRF [13] (marked by \*), respectively. In both cases, our method consistently achieves the highest performance. Fig. 3a shows that our method effectively reduces floaters and appearance distortions compared with other SOTA methods, reinforcing the importance of consistency and diversity as hypothesized.

**LLFF.** Our method achieves a substantial performance improvement over other SOTA approaches, as shown in Tab. 2. This result demonstrates the effectiveness of our method not only on synthetic datasets but also on real-world datasets. As shown in Fig. 3b, our method effectively prevents geometric distortions compared with other methods due to enhanced consistency. Performance with additional views is provided in the supplementary material.

**DTU.** To demonstrate the generalizability of our method, we integrate it with the regularization-based FlipNeRF [34] and the framework-based CVT-xRF [52]. Our DivCon-Flip outperforms the base FlipNeRF in all metrics except SSIM, and our DivCon-CVT achieves SOTA performance, as shown in Tab. 3. Integrating our method with CVT-xRF substantially improves PSNR, SSIM, and AVGE performance while nearly maintaining LPIPS. This result suggests that our method is relatively independent or complementary to framework-based methods. Fig. 3c shows that

Table 1. **Quantitative comparison on Blender.** We compare our method with various NeRF-based approaches. The top three entries are marked in red, orange, and yellow. \* indicates experiments conducted under DietNeRF [13] settings. † indicates that the reported results are taken from the original paper since the official code was not publicly available. The same notation is used in the following tables.

Method	Setting	PSNR $\uparrow$		SSIM $\uparrow$		LPIPS $\downarrow$		AVGE $\downarrow$	
		4-view	8-view	4-view	8-view	4-view	8-view	4-view	8-view
Mip-NeRF [2]	Baselines	14.12	18.74	0.722	0.828	0.382	0.238	0.221	0.121
InfoNeRF [18]	Regularization-based	18.44	22.01	0.792	0.852	0.217	0.120	0.118	0.071
RegNeRF [30]		13.71	19.11	0.786	0.841	0.339	0.193	0.208	0.110
MixNeRF [35]		18.99	23.84	0.807	0.878	0.199	0.103	0.113	0.060
FlipNeRF [34]		20.60	24.38	0.822	0.883	0.159	0.095	0.091	0.055
FreeNeRF* [47]		20.06	24.26	0.815	0.883	0.141	0.082	0.092	0.053
CVT-xRF* [52]	Framework-based	19.98	23.33	0.819	0.874	0.178	0.139	0.096	0.066
mi-MLP* [53]		20.38	24.70	0.828	0.885	0.156 <sup>†</sup>	0.087 <sup>†</sup>	0.084 <sup>†</sup>	0.047 <sup>†</sup>
DivCon-NeRF (Ours)	Regularization-based	22.01	24.85	0.843	0.892	0.127	0.089	0.073	0.047
DivCon-NeRF* (Ours)		22.08	25.10	0.839	0.896	0.129	0.079	0.074	0.045

Table 2. **Quantitative comparison on LLFF under the 3-view setting.** Our method achieves the best performance among SOTA methods. We report fine-tuning (ft) performance for prior-based methods.

Method	Setting	PSNR $\uparrow$	SSIM $\uparrow$	LPIPS $\downarrow$	AVGE $\downarrow$
Mip-NeRF [2]	Baselines	15.53	0.363	0.445	0.223
SRF-ft [7]	Prior-based	17.07	0.436	0.496	0.198
PixelNeRF-ft [48]		16.17	0.438	0.473	0.210
MVSNerF-ft [4]		17.88	0.584	0.260	0.143
DietNeRF [13]	Regularization-based	14.94	0.370	0.423	0.221
RegNeRF [30]		19.08	0.587	0.263	0.132
DS-NeRF [10]		18.12	0.563	0.269	0.145
FlipNeRF [34]		19.34	0.631	0.235	0.123
FreeNeRF [47]		19.63	0.612	0.240	0.122
AR-NeRF [46]		19.90	0.635	0.283 <sup>†</sup>	0.126 <sup>†</sup>
mi-MLP [53]	Framework-based	19.75	0.614	0.300 <sup>†</sup>	0.125 <sup>†</sup>
DivCon-NeRF (Ours)	Regularization-based	20.45	0.660	0.222	0.109

our method produces cleaner renderings than other methods. Performance with additional views is provided in the supplementary material.

### 5.3. Analysis

**Diversity.** We evaluate the impact of ray diversity on rendering quality by progressively expanding the range of  $\theta$ ,  $\phi$ , and  $r$ . As shown in Fig. 4, low diversity results in severe floaters (red boxes), while increased diversity notably reduces these artifacts, indicating the importance of augmented rays from diverse viewpoints. Particularly, when the range of angles is narrow, we observe more floaters and pronounced visual distortions (green boxes). However, using a full viewing angle can lead to challenges in maintaining perfect consistency.

**Absence of consistency mask.** To analyze the importance of consistency, we evaluate the performance of DivCon-NeRF without the consistency mask. In object-centric scenes, as shown in Fig. 5a, reduced consistency leads

Table 3. **Quantitative comparison on DTU under the 3-view setting.** To demonstrate generalizability, we integrate our method separately with FlipNeRF [34] and CVT-xRF [52]. Results are evaluated by masked metrics following [30, 34, 52].

Method	Setting	PSNR $\uparrow$	SSIM $\uparrow$	LPIPS $\downarrow$	AVGE $\downarrow$
Mip-NeRF [2]	Baselines	9.02	0.570	0.339	0.309
SRF-ft [7]	Prior-based	15.68	0.698	0.260	0.160
PixelNeRF-ft [48]		18.95	0.710	0.242	0.121
MVSNerF-ft [4]		18.54	0.769	0.168	0.107
DS-NeRF [10]	Regularization-based	19.48	0.695	0.269	0.121
MixNeRF [35]		18.95	0.744	0.203	0.113
FlipNeRF [34]		19.55	0.767	0.180	0.101
FreeNeRF [47]		19.92	0.787	0.147	0.092
AR-NeRF [46]		20.36	0.788	0.187 <sup>†</sup>	0.095 <sup>†</sup>
CVT-xRF [52]	Framework-based	21.00	0.837	0.132	0.077
DivCon-Flip (Ours)	(Reg.+Reg.)-based	19.91	0.763	0.162	0.096
DivCon-CVT (Ours)	(Reg.+Frame.)-based	22.03	0.858	0.134	0.069

to significant visual distortions. In the depth map, empty spaces appear on the object surfaces, indicating that the rays fail to locate the surface. This result suggests that inconsistent rays are used during training, which increases uncertainty in depth estimation and results in an inability to predict reliable depth values. These results demonstrate the crucial role of consistency in ray augmentation for preventing visual distortions.

As shown in Fig. 5b, diversity alone cannot eliminate many floaters in the LLFF scene with varying depths. In this case, consistency masks effectively reduce floaters and appearance distortions. Therefore, our model performs robustly in synthetic and real-world scenes by enhancing both diversity and consistency.

**Limitations of using rendered depth.** We compare the performance of using the argmax function versus rendered depth to determine the surface point and apply the consistency mask. Notably, using rendered depth results in lower performance, as shown in Tab. 4. This result suggests that

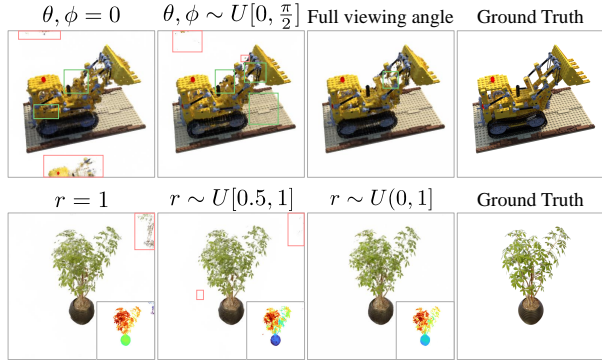


Figure 4. **Analysis of diversity for angle and radius on Blender.** The bottom right of the second row shows depth maps. Best viewed when enlarged.

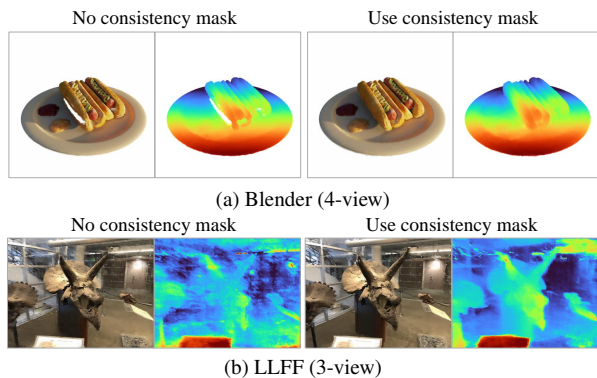


Figure 5. **Comparison of renderings with and without the consistency mask.** We conduct experiments on Blender under the 4-view setting and LLFF under the 3-view setting.

because depth calculation depends on accurate blending weights for all points, using the argmax function for surface point and masking is a more effective way to maintain model consistency during training. Qualitative results can be found in the supplementary material.

**Ablation study.** Tab. 5 presents the ablation study results, showing the impact of each component in our method. In (2), adding only  $\mathcal{L}_{RC}$  to align surface points achieves a noticeable performance improvement, except for SSIM. Incorporating  $\mathcal{L}_{PBF}$  significantly surpasses the baseline across all metrics, as shown in (3). Adding  $\mathcal{L}_{MNLL}$  of inner-sphere augmented rays achieves the best performance in (4), underscoring the importance of enhancing diversity while preserving consistency.

In (5),  $\mathcal{L}_{BF}$  represents the bottleneck feature loss proposed in FlipNeRF [34]. Substituting  $\mathcal{L}_{PBF}$  with  $\mathcal{L}_{BF}$  results in substantial overall performance degradation, indicating the importance of considering the relative positions of points for reliable feature matching.

Table 4. **Comparison of using the argmax function and rendered depth on LLFF.** Using the argmax function is more effective for enhancing consistency.

Methods	PSNR $\uparrow$	SSIM $\uparrow$	LPIPS $\downarrow$
DivCon-NeRF (w/ argmax)	<b>20.45</b>	<b>0.660</b>	<b>0.222</b>
DivCon-NeRF (w/ depth)	19.25	0.607	0.289

Table 5. **Ablation study.** We conduct an ablation study on the Blender dataset with 4 input views.

	Base	$\mathcal{L}_{RC}$	$\mathcal{L}_{PBF}$	$\mathcal{L}_{MNLL}$	$\mathcal{L}_{BF}$	PSNR $\uparrow$	SSIM $\uparrow$	LPIPS $\downarrow$
(1)	✓					18.86	0.803	0.212
(2)	✓	✓				19.60	0.802	0.182
(3)	✓	✓	✓			20.69	0.820	0.168
(4)	✓	✓	✓	✓		<b>22.08</b>	<b>0.839</b>	<b>0.129</b>
(5)	✓	✓		✓	✓	20.73	0.817	0.149



Figure 6. **Qualitative comparison of our method with recent few-shot 3DGS methods on Blender in the 4-view setting.**

#### 5.4. Effectiveness in background-free scenes

Our method is highly effective in object-centric scenes without a background. Fig. 6 shows that even recent few-shot 3DGS methods [50, 54] still suffer from severe distortions and floaters. In contrast, our method exhibits fewer distortions and no floaters. More details can be found in the supplementary material. Therefore, our method is particularly useful for e-commerce and digital advertising, where background-free object visualization is crucial. Our method enables displaying products from multiple angles in a clean, background-free setting, allowing for versatile placement in various advertising environments.

## 6. Conclusion

In this paper, we present DivCon-NeRF, which effectively reduces floaters and visual distortions in few-shot view synthesis. Due to the fine filtering of inconsistent augmented rays by our consistency mask, we are the first to utilize pseudo views from all 360-degree directions based on a virtual sphere. Our method enhances diversity and preserves consistency simultaneously, and we experimentally demonstrate their effects in both object-centric and realistic scenes. This work offers a new perspective on the significance of ray diversity and consistency in few-shot view synthesis.



## References

- [1] Panos Achlioptas, Olga Diamanti, Ioannis Mitliagkas, and Leonidas Guibas. Learning representations and generative models for 3d point clouds. In *International Conference on Machine Learning*, pages 40–49. PMLR, 2018. 2
- [2] Jonathan T Barron, Ben Mildenhall, Matthew Tancik, Peter Hedman, Ricardo Martin-Brualla, and Pratul P Srinivasan. Mip-nerf: A multiscale representation for anti-aliasing neural radiance fields. In *Proceedings of the IEEE/CVF International Conference on Computer Vision*, pages 5855–5864, 2021. 7
- [3] Jonathan T Barron, Ben Mildenhall, Dor Verbin, Pratul P Srinivasan, and Peter Hedman. Mip-nerf 360: Unbounded anti-aliased neural radiance fields. In *Proceedings of the IEEE/CVF Conference on Computer Vision and Pattern Recognition*, pages 5470–5479, 2022. 2
- [4] Anpei Chen, Zexiang Xu, Fuqiang Zhao, Xiaoshuai Zhang, Fanbo Xiang, Jingyi Yu, and Hao Su. Mvsnerf: Fast generalizable radiance field reconstruction from multi-view stereo. In *Proceedings of the IEEE/CVF International Conference on Computer Vision*, pages 14124–14133, 2021. 2, 7
- [5] Di Chen, Yu Liu, Lianghua Huang, Bin Wang, and Pan Pan. Geoaug: Data augmentation for few-shot nerf with geometry constraints. In *Proceedings of the European Conference on Computer Vision*, pages 322–337. Springer, 2022. 3
- [6] Tianlong Chen, Peihao Wang, Zhiwen Fan, and Zhangyang Wang. Aug-nerf: Training stronger neural radiance fields with triple-level physically-grounded augmentations. In *Proceedings of the IEEE/CVF Conference on Computer Vision and Pattern Recognition*, pages 15191–15202, 2022. 3
- [7] Julian Chibane, Aayush Bansal, Verica Lazova, and Gerard Pons-Moll. Stereo radiance fields (srf): Learning view synthesis for sparse views of novel scenes. In *Proceedings of the IEEE/CVF Conference on Computer Vision and Pattern Recognition*, pages 7911–7920, 2021. 7
- [8] Ekin D Cubuk, Barret Zoph, Dandelion Mane, Vijay Vasudevan, and Quoc V Le. Autoaugment: Learning augmentation strategies from data. In *Proceedings of the IEEE/CVF Conference on Computer Vision and Pattern Recognition*, pages 113–123, 2019. 2
- [9] Ekin D Cubuk, Barret Zoph, Jonathon Shlens, and Quoc V Le. Randaugment: Practical automated data augmentation with a reduced search space. In *Proceedings of the IEEE/CVF Conference on Computer Vision and Pattern Recognition Workshops*, pages 702–703, 2020. 2
- [10] Kangle Deng, Andrew Liu, Jun-Yan Zhu, and Deva Ramanan. Depth-supervised nerf: Fewer views and faster training for free. In *Proceedings of the IEEE/CVF Conference on Computer Vision and Pattern Recognition*, pages 12882–12891, 2022. 2, 3, 7
- [11] Matheus Gadelha, Subhransu Maji, and Rui Wang. 3d shape induction from 2d views of multiple objects. In *2017 International Conference on 3D Vision*, pages 402–411. IEEE, 2017. 2
- [12] Dan Hendrycks, Norman Mu, Ekin D Cubuk, Barret Zoph, Justin Gilmer, and Balaji Lakshminarayanan. Augmix: A simple data processing method to improve robustness and uncertainty. *International Conference on Learning Representations*, 2020. 2
- [13] Ajay Jain, Matthew Tancik, and Pieter Abbeel. Putting nerf on a diet: Semantically consistent few-shot view synthesis. In *Proceedings of the IEEE/CVF International Conference on Computer Vision*, pages 5885–5894, 2021. 2, 3, 6, 7
- [14] Ajay Jain, Ben Mildenhall, Jonathan T Barron, Pieter Abbeel, and Ben Poole. Zero-shot text-guided object generation with dream fields. In *Proceedings of the IEEE/CVF Conference on Computer Vision and Pattern Recognition*, pages 867–876, 2022. 2
- [15] Rasmus Jensen, Anders Dahl, George Vogiatzis, Engin Tola, and Henrik Aanaes. Large scale multi-view stereopsis evaluation. In *Proceedings of the IEEE/CVF Conference on Computer Vision and Pattern Recognition*, pages 406–413, 2014. 6
- [16] Mohammad Mahdi Johari, Yann Lepoittevin, and François Fleuret. Geonerf: Generalizing nerf with geometry priors. In *Proceedings of the IEEE/CVF Conference on Computer Vision and Pattern Recognition*, pages 18365–18375, 2022. 2
- [17] Angjoo Kanazawa, Shubham Tulsiani, Alexei A Efros, and Jitendra Malik. Learning category-specific mesh reconstruction from image collections. In *Proceedings of the European Conference on Computer Vision*, pages 371–386. Springer, 2018. 2
- [18] Mijeong Kim, Seonguk Seo, and Bohyung Han. Infonerf: Ray entropy minimization for few-shot neural volume rendering. In *Proceedings of the IEEE/CVF Conference on Computer Vision and Pattern Recognition*, pages 12912–12921, 2022. 3, 5, 7
- [19] Alex Krizhevsky, Ilya Sutskever, and Geoffrey E Hinton. Imagenet classification with deep convolutional neural networks. *Advances in Neural Information Processing Systems*, 25, 2012. 2, 6
- [20] Minseop Kwak, Jiuh Song, and Seungryong Kim. Geconerf: Few-shot neural radiance fields via geometric consistency. In *International Conference on Machine Learning*, 2023. 3, 5
- [21] Ingyun Lee, Wooju Lee, and Hyun Myung. Domain generalization with vital phase augmentation. In *Proceedings of the AAAI Conference on Artificial Intelligence*, pages 2892–2900, 2024. 2
- [22] Jiahe Li, Jiawei Zhang, Xiao Bai, Jin Zheng, Xin Ning, Jun Zhou, and Lin Gu. Dngaussian: Optimizing sparse-view 3d gaussian radiance fields with global-local depth normalization. In *Proceedings of the IEEE/CVF Conference on Computer Vision and Pattern Recognition*, pages 20775–20785, 2024. 3
- [23] Yiyi Liao, Simon Donne, and Andreas Geiger. Deep marching cubes: Learning explicit surface representations. In *Proceedings of the IEEE/CVF Conference on Computer Vision and Pattern Recognition*, pages 2916–2925, 2018. 2
- [24] Chen-Hsuan Lin, Jun Gao, Luming Tang, Towaki Takikawa, Xiaohui Zeng, Xun Huang, Karsten Kreis, Sanja Fidler, Ming-Yu Liu, and Tsung-Yi Lin. Magic3d: High-resolution text-to-3d content creation. In *Proceedings of the IEEE/CVF*

- Conference on Computer Vision and Pattern Recognition*, pages 300–309, 2023. 2
- [25] Ricardo Martin-Brualla, Noha Radwan, Mehdi SM Sajjadi, Jonathan T Barron, Alexey Dosovitskiy, and Daniel Duckworth. Nerf in the wild: Neural radiance fields for unconstrained photo collections. In *Proceedings of the IEEE/CVF Conference on Computer Vision and Pattern Recognition*, pages 7210–7219, 2021. 2
- [26] Ben Mildenhall, Pratul P Srinivasan, Rodrigo Ortiz-Cayon, Nima Khademi Kalantari, Ravi Ramamoorthi, Ren Ng, and Abhishek Kar. Local light field fusion: Practical view synthesis with prescriptive sampling guidelines. *ACM Transactions on Graphics*, 38(4):29:1–29:14, 2019. 5, 6
- [27] Ben Mildenhall, Pratul P. Srinivasan, Matthew Tancik, Jonathan T. Barron, Ravi Ramamoorthi, and Ren Ng. Nerf: Representing scenes as neural radiance fields for view synthesis. In *Proceedings of the European Conference on Computer Vision*, pages 405–421. Springer, 2020. 1, 2, 3, 6
- [28] Ben Mildenhall, Peter Hedman, Ricardo Martin-Brualla, Pratul P Srinivasan, and Jonathan T Barron. Nerf in the dark: High dynamic range view synthesis from noisy raw images. In *Proceedings of the IEEE/CVF Conference on Computer Vision and Pattern Recognition*, pages 16190–16199, 2022.
- [29] Thomas Müller, Alex Evans, Christoph Schied, and Alexander Keller. Instant neural graphics primitives with a multiresolution hash encoding. *ACM Transactions on Graphics*, 41(4):102:1–102:15, 2022. 2
- [30] Michael Niemeyer, Jonathan T Barron, Ben Mildenhall, Mehdi SM Sajjadi, Andreas Geiger, and Noha Radwan. Regnerf: Regularizing neural radiance fields for view synthesis from sparse inputs. In *Proceedings of the IEEE/CVF Conference on Computer Vision and Pattern Recognition*, pages 5480–5490, 2022. 3, 6, 7
- [31] Junyi Pan, Xiaoguang Han, Weikai Chen, Jiapeng Tang, and Kui Jia. Deep mesh reconstruction from single rgb images via topology modification networks. In *Proceedings of the IEEE/CVF Conference on Computer Vision and Pattern Recognition*, pages 9964–9973, 2019. 2
- [32] Keunhong Park, Utkarsh Sinha, Jonathan T Barron, Sofien Bouaziz, Dan B Goldman, Steven M Seitz, and Ricardo Martin-Brualla. Nerfies: Deformable neural radiance fields. In *Proceedings of the IEEE/CVF International Conference on Computer Vision*, pages 5865–5874, 2021. 2
- [33] Ben Poole, Ajay Jain, Jonathan T Barron, and Ben Mildenhall. Dreamfusion: Text-to-3d using 2d diffusion. In *International Conference on Learning Representations*, 2022. 2
- [34] Seunghyeon Seo, Yeonjin Chang, and Nojun Kwak. Flipnerf: Flipped reflection rays for few-shot novel view synthesis. In *Proceedings of the IEEE/CVF International Conference on Computer Vision*, pages 22883–22893, 2023. 2, 3, 5, 6, 7, 8
- [35] Seunghyeon Seo, Donghoon Han, Yeonjin Chang, and Nojun Kwak. Mixnerf: Modeling a ray with mixture density for novel view synthesis from sparse inputs. In *Proceedings of the IEEE/CVF Conference on Computer Vision and Pattern Recognition*, pages 20659–20668, 2023. 2, 3, 6, 7
- [36] Nagabhushan Somraj and Rajiv Soundararajan. Vip-nerf: Visibility prior for sparse input neural radiance fields. In *ACM SIGGRAPH 2023 Conference Proceedings*, pages 71:1–71:11, 2023. 2
- [37] Hugues Thomas, Charles R Qi, Jean-Emmanuel Deschaud, Beatriz Marcotegui, François Goulette, and Leonidas J Guibas. Kpconv: Flexible and deformable convolution for point clouds. In *Proceedings of the IEEE/CVF Conference on Computer Vision and Pattern Recognition*, pages 6411–6420, 2019. 2
- [38] Prune Truong, Marie-Julie Rakotosaona, Fabian Manhardt, and Federico Tombari. Sparf: Neural radiance fields from sparse and noisy poses. In *Proceedings of the IEEE/CVF Conference on Computer Vision and Pattern Recognition*, pages 4190–4200, 2023. 3
- [39] Ashish Vaswani, Noam Shazeer, Niki Parmar, Jakob Uszkoreit, Llion Jones, Aidan N Gomez, Łukasz Kaiser, and Illia Polosukhin. Attention is all you need. In *Advances in Neural Information Processing Systems*, 2017. 2
- [40] Guangcong Wang, Zhaoxi Chen, Chen Change Loy, and Ziwei Liu. Sparsenerf: Distilling depth ranking for few-shot novel view synthesis. In *Proceedings of the IEEE/CVF Conference on Computer Vision and Pattern Recognition*, pages 9065–9076, 2023. 3
- [41] Qianqian Wang, Zhicheng Wang, Kyle Genova, Pratul P Srinivasan, Howard Zhou, Jonathan T Barron, Ricardo Martin-Brualla, Noah Snavely, and Thomas Funkhouser. Ibrnet: Learning multi-view image-based rendering. In *Proceedings of the IEEE/CVF Conference on Computer Vision and Pattern Recognition*, pages 4690–4699, 2021. 2
- [42] Zhou Wang, Alan Bovik, Hamid Sheikh, and Eero Simoncelli. Image quality assessment: From error visibility to structural similarity. *IEEE Transactions on Image Processing*, 13(4):600–612, 2004. 6
- [43] Jiajun Wu, Chengkai Zhang, Tianfan Xue, Bill Freeman, and Josh Tenenbaum. Learning a probabilistic latent space of object shapes via 3d generative-adversarial modeling. *Advances in Neural Information Processing Systems*, 29, 2016. 2
- [44] Haozhe Xie, Hongxun Yao, Xiaoshuai Sun, Shangchen Zhou, and Shengping Zhang. Pix2vox: Context-aware 3d reconstruction from single and multi-view images. In *Proceedings of the IEEE/CVF International Conference on Computer Vision*, pages 2690–2698, 2019. 2
- [45] Qizhe Xie, Zihang Dai, Eduard Hovy, Thang Luong, and Quoc Le. Unsupervised data augmentation for consistency training. *Advances in Neural Information Processing Systems*, 33:6256–6268, 2020. 2
- [46] Qingshan Xu, Xuanyu Yi, Jianyao Xu, Wenbing Tao, Yew-Soon Ong, and Hanwang Zhang. Few-shot nerf by adaptive rendering loss regularization. In *Proceedings of the European Conference on Computer Vision*. Springer, 2024. 7
- [47] Jiawei Yang, Marco Pavone, and Yue Wang. Freenerf: Improving few-shot neural rendering with free frequency regularization. In *Proceedings of the IEEE/CVF Conference on Computer Vision and Pattern Recognition*, pages 8254–8263, 2023. 2, 3, 7
- [48] Alex Yu, Vickie Ye, Matthew Tancik, and Angjoo Kanazawa. Pixelnerf: Neural radiance fields from one or few images.

In *Proceedings of the IEEE/CVF Conference on Computer Vision and Pattern Recognition*, pages 4578–4587, 2021. [2](#), [7](#)

- [49] Alex Yu, Sara Fridovich-Keil, Matthew Tancik, Qinhong Chen, Benjamin Recht, and Angjoo Kanazawa. Plenoxels: Radiance fields without neural networks. In *Proceedings of the IEEE/CVF Conference on Computer Vision and Pattern Recognition*, pages 5501–5510, 2022. [2](#)
- [50] Jiawei Zhang, Jiahe Li, Xiaohan Yu, Lei Huang, Lin Gu, Jin Zheng, and Xiao Bai. Cor-gs: Sparse-view 3d gaussian splatting via co-regularization. In *Proceedings of the European Conference on Computer Vision*, pages 335–352. Springer, 2024. [3](#), [8](#)
- [51] Richard Zhang, Phillip Isola, Alexei A Efros, Eli Shechtman, and Oliver Wang. The unreasonable effectiveness of deep features as a perceptual metric. In *Proceedings of the IEEE/CVF Conference on Computer Vision and Pattern Recognition*, pages 586–595, 2018. [6](#)
- [52] Yingji Zhong, Lanqing Hong, Zhenguo Li, and Dan Xu. Cvt-xrf: Contrastive in-voxel transformer for 3d consistent radiance fields from sparse inputs. In *Proceedings of the IEEE/CVF Conference on Computer Vision and Pattern Recognition*, pages 21466–21475, 2024. [2](#), [6](#), [7](#)
- [53] Hanxin Zhu, Tianyu He, Xin Li, Bingchen Li, and Zhibo Chen. Is vanilla mlp in neural radiance field enough for few-shot view synthesis? In *Proceedings of the IEEE/CVF Conference on Computer Vision and Pattern Recognition*, pages 20288–20298, 2024. [2](#), [7](#)
- [54] Zehao Zhu, Zhiwen Fan, Yifan Jiang, and Zhangyang Wang. Fsgs: Real-time few-shot view synthesis using gaussian splatting. In *Proceedings of the European Conference on Computer Vision*, pages 145–163. Springer, 2024. [3](#), [8](#)